Heliyon 9 (2023) e15502

Contents lists available at ScienceDirect

Heliyon

journal homepage: www.cell.com/heliyon

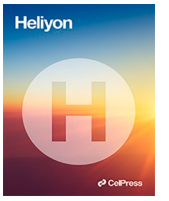

Research article

Removal of methylene blue using MnO_2@rGO nanocomposite from textile wastewater: Isotherms, kinetics and thermodynamics studies

Tshimangadzo S. Munonde [a,b], Azile Nqombolo [a,b,d], Siphosethu Hobongwana [b], Anele Mpupa [a,b], Philiswa Nosizo Nomngongo [a,b,c,*]

[a] Department of Chemical Sciences, University of Johannesburg, Doornfontein Campus, P.O. Box 17011, Doornfontein, 2028, South Africa
[b] Department of Science and Innovation-National Research Foundation South African Research Chair Initiative (DSI-NRF SARChI) in Nanotechnology for Water, University of Johannesburg, Doornfontein, 2028, South Africa
[c] DSI/Mintek Nanotechnology Innovation Centre, University of Johannesburg, Doornfontein, 2028, South Africa
[d] Department of Chemistry, University of Fort Hare, Private Bag X1314, Alice 5700, South Africa

ARTICLE INFO

Keywords:
Chemisorption
Isotherms
Kinetics
Methylene blue
MnO_2@rGO nanocomposite
Textile wastewater

ABSTRACT

In this study, the adsorptive removal of methylene blue dye, which is commonly used in textile industries, was investigated using the MnO_2@reduced graphene oxide (rGO) adsorbent. The sonication-assisted synthesis from rGO nanosheets and MnO_2 nanoparticles resulted to the MnO_2@rGO nanocomposite with improved physicochemical properties. The characterization results showed the improved surface area, porous structure and adsorption sites from the nitrogen adsorption-desorption studies, improved morphology from the Scanning Electron Microscope (SEM) and Transmission Electron Microscope (TEM) and the improved crystal structure from X-ray powder diffraction (XRD). The improved physicochemical properties on the MnO_2@rGO nanocomposite played a significant role in enhancing the dye removal in textile wastewater. The equilibrium experimental data was best described by the Langmuir isotherm model with a maximum adsorption capacity of 156 mg g^{-1}, suggesting a monolayer adsorption. The kinetic data best fitted the pseudo-second order kinetic model, suggesting a chemisorption adsorption process. The thermodynamic data (ΔG°, ΔH° and ΔS°) confirmed the feasibility, randomness and spontaneous nature of the adsorption process. The mechanism of adsorption involved the hydrogen bonding, π-π interactions and electrostatic interactions. The removal of methylene blue using MnO_2@rGO nanocomposite in spiked textile wastewater yielded a 98–99% removal. The method demonstrated competitiveness when compared with literature reported results, paving way for further investigations towards industrial scale applications.

1. Introduction

The textile industry is one of the largest industrial sectors which accounts for about one-fifth of worldwide industrial water pollution [1]. Commonly, a broad range of synthetic materials are used in the textile industry, associating the industry with the

* Corresponding author.Department of Chemical Sciences, University of Johannesburg, Doornfontein Campus, P.O. Box 17011, Doornfontein, 2028, South Africa.
E-mail address: pnnomngongo@uj.ac.za (P.N. Nomngongo).

https://doi.org/10.1016/j.heliyon.2023.e15502
Received 19 August 2022; Received in revised form 6 April 2023; Accepted 11 April 2023
Available online 17 April 2023

excessive use of chemicals, in addition to water and energy [2]. Subsequently, post the textile processes, the discharged textile wastewater usually contains a variety of dye molecules that are harmful, thus posing a serious threat to the environment [3]. Methylene blue (MB), a commonly used thiazine cationic dye known to be stable in water at room temperature, remains as one of the toxic dyes usually found in textile wastewater [4]. As methylene blue is used significantly as a colourant in textile industries, the threat to the environment escalates [5]. To circumvent this threat, the discharged textile effluent has to be treated within the industries before being discharged into the environment.

Meanwhile, MB dye molecules, and other dyes, in the textile wastewater pose challenges to the treatment processes, as they are difficult to biodegrade or photodegrade [6]. Thus, common conventional methods such as oxidation processes, microbial treatment, ozonation, photocatalysis, cloud point extraction, coagulation, and nanofiltration have yielded unsatisfactory results when explored for the removal of dyes in wastewater [7–9]. The adsorption method, however, has shown significant potential as a method of choice for the removal of MB and other various dyes, specifically due to the fast adsorption kinetics, simplicity in design and operation, and low cost [10].

Notably, adsorption equilibria data is the most significant segment of data needed to understand an adsorption process [11]. Thus, the interaction between the adsorbent and the adsorbate dye solutions at equilibria is key to the adsorption process. Various adsorbents have been engineered with the key goal of specifically interacting with the target MB dye molecules based on the possible surface chemistry existing between the adsorbent and MB dye molecule [12–15]. Tuning/engineering the surface area, active sites, electronic conductivity and porous structure are key to the development of adsorbents that are specific to the target MB dye molecule [16]. Interestingly, engineered nanocomposites have been shown to interact well with dye molecules based on these deliberations.

Reduced graphene oxide (rGO) is an economically favoured form of graphene used to manufacture graphene based nanocomposites for various applications. Various synthetic routes such as chemical, photo-chemical, microwave, thermal, photo-thermal and microbial/bacterial processes have been used to produce large yields of rGO [17]. However, the thermal process has become the most attractive route for rGO production due to simplicity and low cost [18]. In this method, graphene oxide (GO) is prepared from graphite using the modified Hummers' method and the sonication-assisted exfoliation to form single/few layers of GO. The single/few layers of GO are then thermally heated at moderately higher temperatures to form rGO of higher quality at a relatively short time, without using any harsh chemicals [19].

Reduced graphene oxide has attracted significant interests for the adsorption of various dyes in aqueous solutions. For instance, Jahan et al. [20] compared the removal of MB on GO and rGO materials, with GO removing 98.67% of the MB dye within 4 h against 93.47% removal by rGO within 7 h. However, the stability and reusability of GO was very low, compared rGO due to the presence of various expandable oxygen atoms on GO than in rGO. It is noteworthy that although rGO nanosheets possess interesting electronic structures that allow them to interact strongly with organic dyes through various covalent and non-covalent forces, they suffer from nanosheets stacking leading to aggregation which reduces their adsorption capabilities [21–23]. However, integrating rGO nanosheets with metal oxides allows for the retention of single-thinned rGO layers with improved adsorption sites, surface area and reduced aggregation/agglomeration [24,25]. Nevertheless, Adel et al. [26] prepared the magnetic $MgFe_2O_4$/reduced graphene oxide that was deployed for the removal of MB in aqueous solutions, with a removal efficiency of 98% in 60 min. Although the magnetism of $MgFe_2O_4$ was important for the easy separation of the adsorbent from the adsorbate, the composite showed poor reusability due to the agglomeration of the magnetic nanoparticles. The adsorption capacity was also very low due to the agglomeration of the magnetic $MgFe_2O_4$ nanoparticles. Thus, the eco-friendly, low cost, stable and abundant MnO_2 nanoparticles appear to reduce the agglomeration state of rGO whilst adding more active sites for adsorption.

In this study, the integration of rGO nanosheets with MnO_2 nanoparticles has shown to improve the physicochemical properties such as the surface area, active sites and porous structure as reflected on the Nitrogen adsorption-desorption studies. The electron conductivity was also uncovered on the XRD analysis, making MnO_2@rGO nanocomposite a potential adsorbent for the removal of MB dye in aqueous solutions. Subsequent to the optimization studies, the equilibrium data was used to evaluate the adsorption characteristics such as the adsorption kinetics, isotherms, thermodynamics, as well as the adsorption mechanism. The study further investigated the removal of MB from spiked textile industrial wastewater using MnO_2@rGO nanocomposite adsorbent under optimum conditions.

2. Experimental procedure

2.1. Reagents and materials

Analytical reagent grade chemicals and double distilled water were used in all the experiments. Methylene blue dye, graphite powder, potassium permanganate ($KMnO_4$), manganese chloride hexahydrate ($MnCl_2{\cdot}6H_2O$), sulphuric acid (H_2SO_4), phosphoric acid (H_3PO_4), hydrochloric acid (HCl), hydrogen peroxide (H_2O_2), diethyl ether and absolute ethanol were all purchased from Sigma-Aldrich (St. Louis, MO, USA).

2.2. Synthesis of rGO nanosheets

The synthesis of rGO followed the previous method by Mnyipika et al. [27] with minor modifications. Initially, graphene oxide (GO) was prepared using the modified hummers' method. To this end, H_2SO_4 and H_3PO_4 were mixed in a ratio 9:1 (360 mL: 40 mL, v/v) prior stirring for 30 min in an ice bath. To this solution, graphite powder (3.14 g) and $KMnO_4$ (18.33 g) were added to the afore-prepared solution under stirring. The mixture was transferred to an oil bath and heated to 85 °C overnight. Then, 200 mL of ice

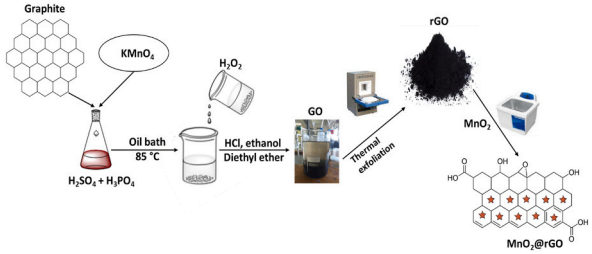

Scheme 1. Schematic illustration for the preparation of the MnO_2@rGO nanocomposite.

water was added, before the reaction was terminated using 20 mL H_2O_2 slowly added to mixture. An exothermic reaction occurred, and the solution was allowed to cool down. Then, 50 mL of 1 M HCl solution was added prior centrifugation, followed by washing with 200 mL ethanol and 200 mL diethyl ether. The product was then dried in an oven at 80 °C for 12 h. Then, GO was converted to rGO by thermal exfoliation at 500 °C on a muffle furnace with a heating rate of 2 °C min^{-1} for 2 h.

2.3. Synthesis of MnO_2 nanoparticles

The synthesis of manganese oxide followed a drop-feeding method previously reported by Yogambicha et al. [28], with minor modifications. In a beaker, 18.55 g manganese chloride hexahydrate was dissolved in 50 mL deionized water and stirred for 30 min. Then, 10 mL of ethanol was added to the solution and allowed to stir for a further 10 min. In a separate beaker, 9.89 g potassium permanganate was also dissolved in 50 mL deionized water and stirred for 30 min. The potassium permanganate solution in the second beaker was then added dropwise to the solution in the first beaker forming a black precipitate. The precipitate was then centrifuged and washed with ethanol, before being dried in an oven at 110 °C overnight.

2.4. Synthesis of MnO_2@rGO nanocomposite

The MnO_2@rGO nanocomposite was prepared by dispersing 1.14 g rGO in 200 mL of ethylene glycol in an ultrasound sonicater for 1 h. To this colloidal solution, 1.12 g of MnO_2 was added, and the solution was ultrasonicated for a further 1 h. The product was washed with deionized water and twice with ethanol under centrifugation, and then dried in an oven at 100 °C for 12 h. The overall synthesis of the MnO_2@rGO nanocomposite is illustrated in Scheme 1.

2.5. Characterization of the synthesized materials

High resolution Transmission electron microscopy (JEM-2100, JEOL, Tokyo, Japan) and field-emission scanning electron microscopy/energy dispersive X-ray spectroscopy (EDS) (TESCAN VEGA 3 XMU, LMH instrument, Czech Republic) were used to study the morphology of the prepared nanomaterials. EDS was operated at an accelerating voltage of 20 kV for elemental analysis. Fourier transform infrared spectrum was recorded in the range 4000–400 cm^{-1} on a PerkinElmer spectrum 100 Fourier transform infrared spectrometer (Waltham, MA, USA). The crystal structures of the prepared nanomaterials were evaluated on a Rigaku Ultima IV X-ray diffractometer using a Cu-K_α radiation with a wavelength of 0.154 nm. Nitrogen adsorption-desorption studies were carried out on a Tristar II instrument (Micromeritics, Norcross, GA, USA). Prior measuring the BET properties using nitrogen gas at 77 K, the samples were degassed at 110 °C for 16.5 h. The H1 9811-5, pH meter (HANNA Instruments, Smithfield, RI, USA) was used for all pH measurements.

2.6. Equilibrium studies of batch adsorption experiments

The batch adsorption experiments were executed on an ultrasound cleaner (703 Scientech ultrasonic cleaner, Rochelle lab equipment, South Africa) with voltage = 230 V-50 Hz and a power of 150 W at mild frequencies for 60 min at a temperature range of 25–40 °C (adjusted by cooling the ultrasound cleaner with ice cubes). The method was optimized using a central composite design, with key independent factors such as sample pH, sample dosage and sonication power investigated, as presented in Tables S1 and S2. Essentially, the batch adsorption experiments were carried out by weighing appropriate amounts of the adsorbent in 100 mL conical flasks, followed by the addition of 50 mL of the prepared 30 mg L^{-1} methylene blue solution prior to sonication in an ultrasound cleaner. Afterwards, 3–5 mL of the solutions were filtered using 0.22 μm PVDF filters prior to analysis with an ultraviolet–visible spectrophotometer (UV–Vis 180, Thermofischer) at a predetermined absorption wavelength of 625 nm. The UV–Vis spectrophotometer was initially calibrated using the prepared methylene blue working standard solution with concentrations of 0, 5, 10, 20, 30, 40, 50 and 60 mg L^{-1} from a 100 mg L^{-1} stock solution that was diluted with deionized water. The calibration curve was plotted using the absorbance and concentration of the dye solution obtained at the absorption wavelength of 625 nm, with the coefficient of determination (r^2) of 0.9999, suggesting a perfectly linear calibration. The concentrations in the samples were then determined against the prepared calibration curve by directly running the samples on the UV–Vis and the readings of the concentrations obtained from the

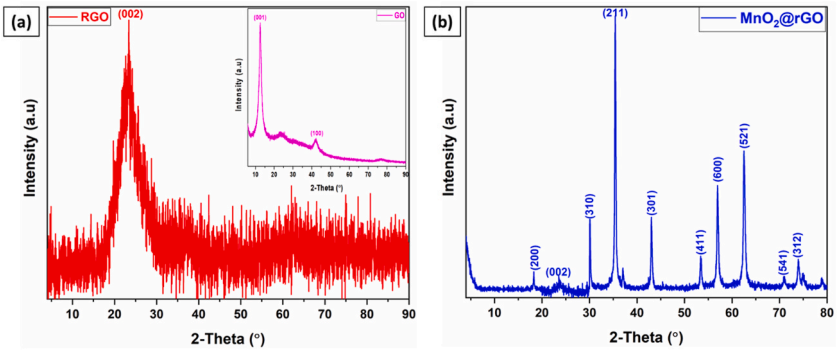

Fig. 1. XRD spectra of rGO nanosheets (a) and MnO_2@rGO nanocomposite (b).

instrument [29,30]. The adsorption removal efficiency, adsorption capacity at equilibrium (q_e) and adsorption capacity at time t were determined using equations (1)–(3).

$$\% RE = \frac{(C_0 - C_e)}{C_0} * 100 \tag{1}$$

$$q_e = \frac{(C_0 - C_e)\, V}{m} \tag{2}$$

$$q_t = \frac{(C_0 - C_t)\, V}{m} \tag{3}$$

where: %RE = removal efficiency, C_0 and C_e represent the initial concentration (mg L^{-1}) and equilibrium concentration (mg L^{-1}) respectively, V = volume of aqueous solution (L), m = mass of the adsorbent (g), q_e and q_t represent adsorption capacity at equilibrium (mg g^{-1}) and adsorption capacity at time t (mg g^{-1}).

Under optimum conditions, the equilibrium adsorption isotherms were studied in triplicates at a concentration range of 10–160 mg L^{-1} and the adsorption capacity was calculated using equation (2). Furthermore, the equilibrium adsorption kinetics were investigated in triplicates in the time range of 1–60 min, with the adsorption capacity at time t calculated using equation (3).

2.7. Sample collection and analysis

The influent and effluent wastewater were collected from a textile industry in KwaZulu-Natal using pre-cleaned plastic containers and stored in the refrigerator at 4 °C prior analysis. The textile wastewater was found to contain 2.34 mg L^{-1} and 3.19 mg L^{-1} of methylene blue in influent and effluent wastewater, respectively. These concentrations were considered when adsorption experiments were carried out for the textile wastewater samples analysis. The accuracy of the developed adsorption method was studied using the spike and recovery method. The procedure was carried out by adjusting the pH of the wastewater solutions (using hydrochloric acid and sodium hydroxide) to 1.55, and then preparing a MB dye solution of a concentration of 30 ± 1.04 mg L^{-1} before using the prepared solutions on the previously developed batch adsorption process.

3. Results and discussion

3.1. X-ray powder diffraction (XRD)

Insights on the crystallographic structures of rGO nanosheets and MnO_2@rGO nanocomposite were deliberated, as shown in Fig. 1. The XRD pattern in Fig. 1(a) shows a broad peak around 26.6° representing the amorphous (002) plane of the rGO nanosheets [31,32]. The XRD pattern of rGO was compared to the GO pattern (inset graph in Fig. 1(a)) which shows the (001) plane around 10° whilst rGO shows the (002) plane around 26°, confirming that the reduction of GO to rGO was successful, and agreed with the literature reports [33,34]. The XRD pattern of the MnO_2@rGO nanocomposite (Fig. 1(b)) displayed the characteristic peaks of MnO_2 nanoparticles at 2θ = 18.2°, 30.2°, 35.3°, 43.1°, 53.5°, 56.9°, 62.5°, 71.1°, and 73.8° corresponding to the (200), (310), (211), (301), (411), (600), (521), (541) and (312) crystalline planes [28,35,36]. The sharp intense MnO_2 nanoparticles peaks clearly show the high crystallinity of the prepared material. Evidently, the (002) broad peak observed around 23.6° corresponding to the rGO nanosheets appear to have shifted significantly, suggesting the change in rGO crystal structure owing to the formation of the MnO_2@rGO nanocomposite [27,35]. It is anticipated that the incorporation of the MnO_2 nanoparticles on the crystal structure of the rGO nanosheets would improve the overall crystallinity of the nanocomposite and therefore the conductivity due to higher order [37,38].

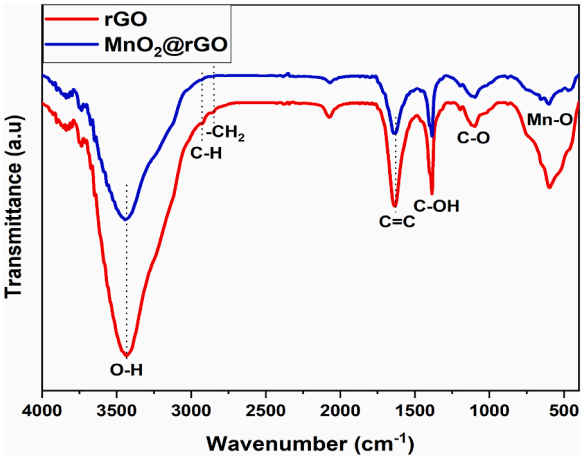

Fig. 2. FTIR spectra of rGO nanosheets (a) and MnO_2@rGO nanocomposite (b).

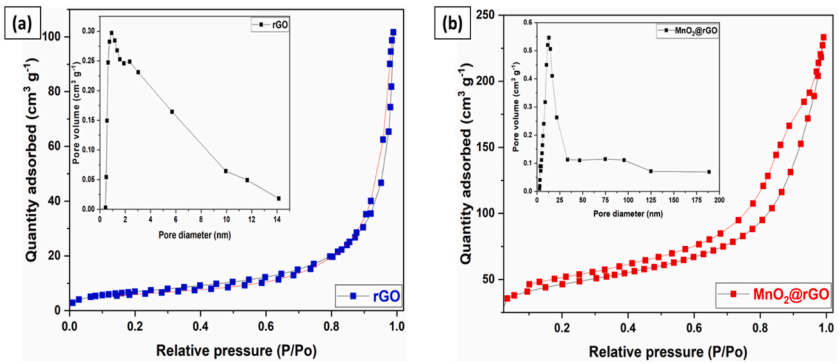

Fig. 3. N_2 adsorption-desorption isotherms for rGO nanosheets (a) and MnO_2@rGO nanocomposite (b).

3.2. *Fourier transform infrared spectroscopy (FTIR)*

To identify the chemical bonds that are present in the rGO and MnO_2@rGO nanocomposite, FTIR spectra is shown in Fig. 2. The bands observed around 3440 cm^{-1} in both spectra can be ascribed to the –OH stretching vibration of absorbed water molecules [28]. The bands observed around 2928 cm^{-1} and 2848 cm^{-1} can be attributed to –CH and –CH_2 of the rGO nanostructure [27], respectively. Furthermore, the stretching bands observed around 1640 cm^{-1}, 1384 cm^{-1} and 1105 cm^{-1} can be attributed to the stretching C═C, hydroxy C–OH and epoxy C–O of the carbon backbone in rGO [39], respectively. Due to the grafting of MnO_2 on rGO, the Mn–O bands are observed around 468 cm^{-1}, 605 cm^{-1} and 661 cm^{-1}, confirming the successful integration of MnO_2 nanoparticles on the rGO nanostructure [24,25,27,28].

3.3. *N_2 adsorption-desorption studies*

To evaluate the surface characteristics of the prepared materials, the N_2 adsorption-desorption isotherms of rGO nanosheets and modified MnO_2@rGO nanocomposite were studied as shown in Fig. 3. The MnO_2@rGO nanocomposite clearly display a type IV isotherm with an H_3-type hysteresis loop in the range 0.7–1.0 (P/Po), which suggests the presence of mesopores [27]. The constant C obtained from the BET equation of 122.53 further confirmed the mesoporous structure of the MnO_2@rGO nanocomposite [40–42]. On the other end, the rGO nanosheets displayed a curve with the resemblance of a type IV and a type I porous structure. However, the constant C obtained from the BET equation was 174.97, confirming the type I microporous structure [40–42]. Furthermore, the Barrett-Joyner-Halenda (BJH) analysis was employed to study the pore size distribution as shown on the inset graphs in Fig. 3a and b. The IUPAC classification of porous materials is centered around three different types namely, macroporous (>50 nm), mesoporous (2–50 nm) and microporous (<2 nm) [43]. Thus, the BJH pore size distribution of the MnO_2@rGO nanocomposite ranged from mesoporous to macroporous [44], with the average pore size of 12.8 nm, as shown in the inset graph in Fig. 3b. The results agree with the previously reported literature results [45–47]. The BJH pore size distribution of the rGO nanoparticles ranged from microporous to mesoporous, with an average pore size of 1.12 nm, suggesting a microporous structure [48,49]. The pore size distribution points of both materials were centered around the average pore size, suggesting the reliability of the average pore size that was used to

Table 1
BET properties of rGO nanosheets and MnO_2@rGO nanocomposite.

Surface properties	rGO nanosheets	MnO_2@rGO nanocomposite
BET surface area ($m^2\ g^{-1}$)	54.46	159.32
Average pore size (nm)	1.12	12.81
Total pore volume ($cm^3\ g^{-1}$)	0.29	0.54

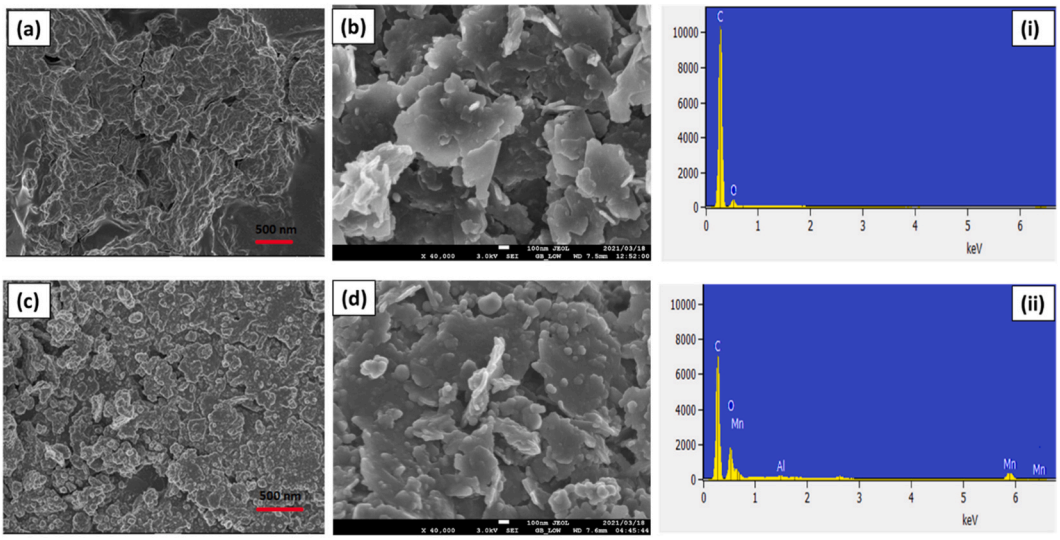

Fig. 4. FE-SEM of rGO nanosheets (a and b) and MnO_2@rGO nanocomposite (c and d), with corresponding EDX spectra of rGO nanosheets (i) and MnO_2@rGO nanocomposite (ii).

Table 2
EDX elemental representation of rGO nanosheets.

Element line	Weight %	Weight % Error	Atom %	Atom % Error
C K	84.04	±0.31	93.96	±0.35
O K	15.96	±0.33	6.04	±0.27
Total	100.00		100.00	

determine the overall pore structure. The surface properties were further summarized in Table 1. It can be perceived that the BET surface area of rGO nanosheets increased from 54.46 $m^2\ g^{-1}$ to 159.32 $m^2\ g^{-1}$ after the surface modification with MnO_2 nanoparticles. Expectedly, the surface improved MnO_2@rGO nanocomposite also displayed an increased pore size and pore volume compared to the rGO nanosheets as shown in Table 1, indicating that the surface grafting of MnO_2 nanoparticles onto rGO nanosheets significantly improved the surface chemistry of the formed MnO_2@rGO nanocomposite [50].

3.4. Field emission scanning electron microscope/energy dispersive X-ray spectroscopy (FE-SEM/EDX)

The morphology of the rGO nanosheets and MnO_2@rGO nanocomposite were studied using FE-SEM and presented in Fig. 4. As expected, Fig. 4(a and b) display the flat nanosheets of rGO, with an average thickness of about 3–4.5 nm, and a lateral dimension in the range of several hundred nanometres. The anticipated microporous nature of the rGO nanosheets can be visualized in Fig. 4a, as discussed in the N_2 adsorption-desorption results. Subsequently, the MnO_2@rGO nanocomposite in Fig. 4(c and d) display the rGO flat nanosheets with spherical MnO_2 nanoparticles embedded on the surface of the nanosheets, with an increased thickness of about 4.7–6.3 nm. The expected mesopores in the MnO_2@rGO nanocomposite can be visualized in Fig. 4c, agreeing with the N_2 adsorption-desorption results. Although the N_2 adsorption-desorption results have shown the BET surface area to have increased, the rGO nanosheets appear to be more agglomerated due to the integration with MnO_2 nanoparticles and therefore shows a much-increased thickness and lateral dimensions in the MnO_2@rGO nanocomposite. The EDX elemental composition confirmed the successful synthesis of RGO with a high carbon content of 84%, and the remaining percentage being oxygen, as displayed in Fig. 4(i) and Table 2. Likewise, the EDX spectrum of MnO_2@rGO nanocomposite (Fig. 4(ii) and Table 3) shows the existence of carbon (47%), O (24%) and Mn (27%), confirming the successful integration of MnO_2 nanoparticles on the rGO nanosheet structure. Al observed in both EDX spectra was due to the sample' contact with the specimen stubs.

Table 3
EDX elemental representation of MnO_2@rGO nanocomposite.

Element line	Weight %	Weight % Error	Atom %	Atom % Error
C K	47.38	±0.48	76.24	±0.70
O K	24.87	±0.13	11.69	±0.14
Al K	0.14	±0.04	0.29	±0.03
Mn K	27.61	±0.74	8.79	±0.23
Mn L	–	–	–	–
Total	100.00		100.00	

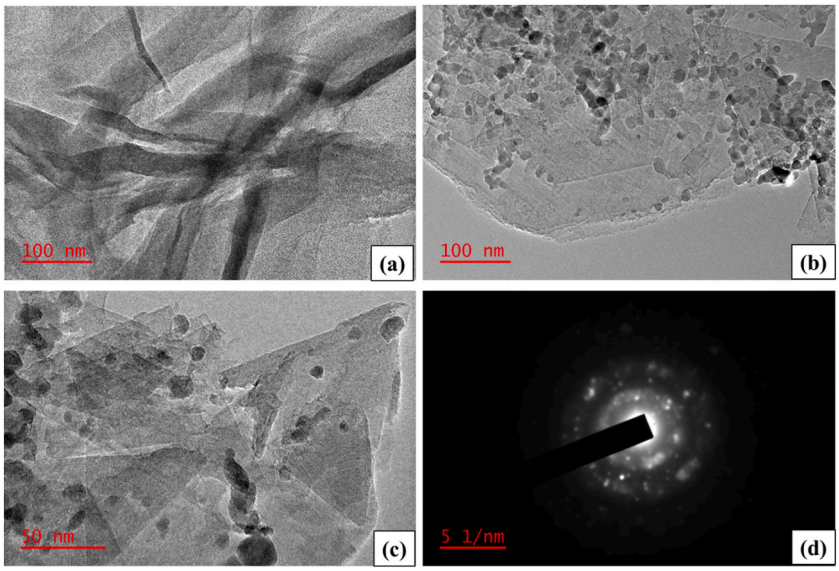

Fig. 5. TEM of MnO_2@rGO nanocomposite (a–c), with corresponding SAED pattern (d).

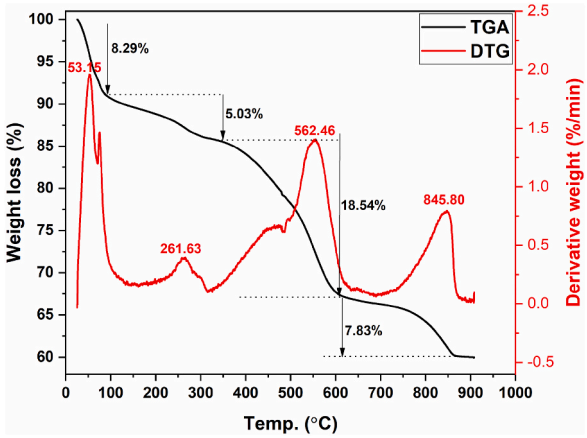

Fig. 6. Thermal analysis curves (TGA and DTG) of MnO_2@rGO nanocomposite.

3.5. *Transmission electron microscope/selected area electron diffraction (TEM/SAED)*

Further insights on the morphology of MnO_2@rGO nanocomposite were deliberated using TEM as presented in Fig. 5. The TEM image in Fig. 5(a) unravels the structure of the rGO flat nanosheets which are slightly agglomerated. The TEM image in Fig. 5(b) shows the spherically shaped MnO_2 nanoparticles embedded on the flat rGO nanosheets. The spherical MnO_2 nanoparticles are well distributed across the rGO surface, suggesting that there would be abundant active sites for adsorption [36,50]. The HR-TEM in Fig. 5 (c) also clearly visualizes and confirms the distribution of the evenly spherically shaped MnO_2 nanoparticles across the rGO

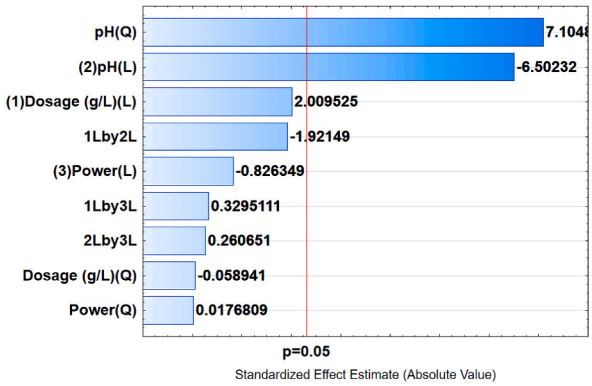

Fig. 7. Pareto Chart of standardized effects generated using a CCD for the adsorption of methylene blue onto MnO_2@rGO. (For interpretation of the references to colour in this figure legend, the reader is referred to the Web version of this article.)

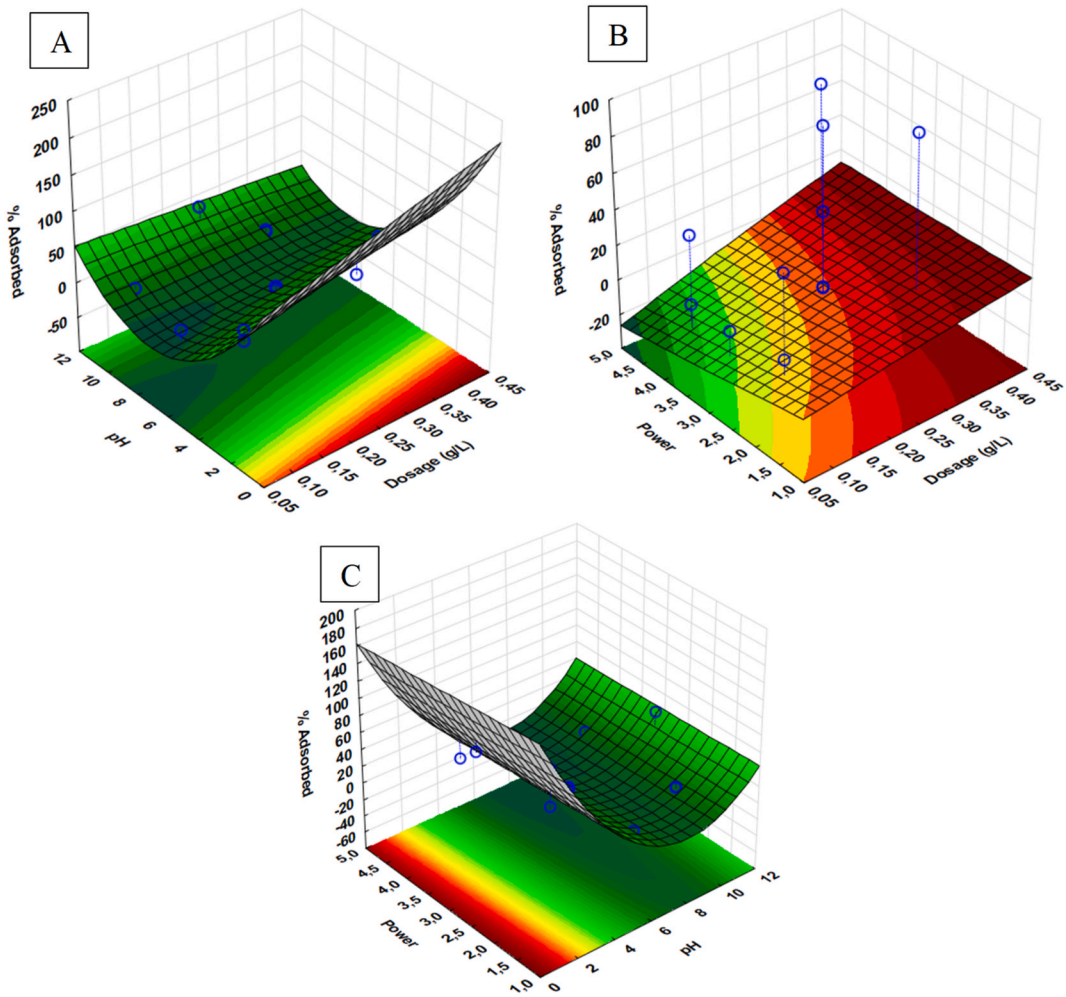

Fig. 8. Three-dimensional surface plots showing the interactive effects of (a) sample pH and adsorbent dosage, (b) sonication power-adsorbent dosage and (c) sonication power and sample pH on the adsorptive removal of methylene blue. (For interpretation of the references to colour in this figure legend, the reader is referred to the Web version of this article.)

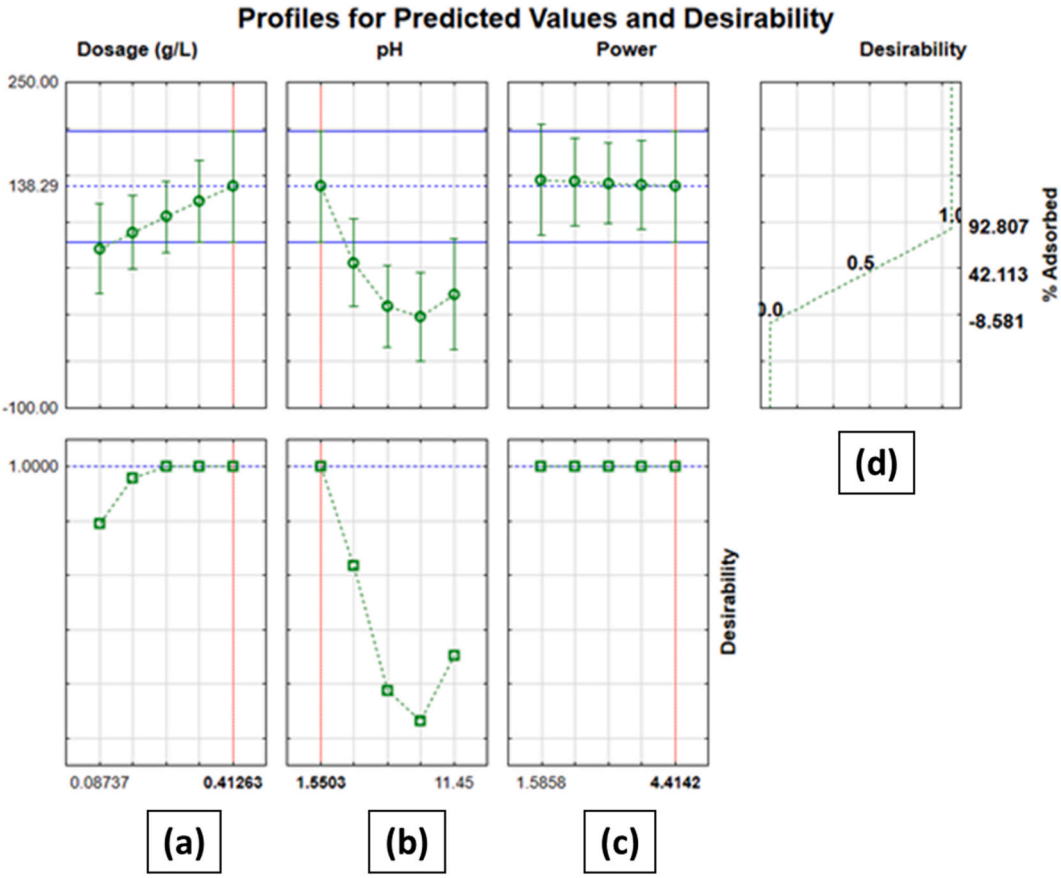

Fig. 9. Desirability profiles and predicted values for optimum conditions: Dosage profile (a), pH profile (b), Sonication power profile (c), and the most desirable percentage adsorption profile (d).

nanosheets. Interestingly, the SAED pattern in Fig. 5(d) shows multiple polyatomic rings showing the characteristics of both rGO nanosheets and MnO_2 nanoparticles. The first two polyatomic rings show multiple bright spots confirming the adherence of MnO_2 nanoparticles on the last two less visible rGO amorphous rings [27,50]. It is noteworthy that the bright spots indicate the high crystallinity of the MnO_2 nanoparticles [36,50]. The two MnO_2 nanoparticles polyatomic rings correspond to the (211) and (521) facets on the XRD, whereas the two amorphous rGO nanosheets rings correspond to the (002) facet, corroborating with the XRD results.

3.6. Thermogravimetric analysis (TGA)/derivative thermogravimetry (DTG)

The thermal analysis of MnO_2@rGO nanocomposite was studied, with the TGA and DTG curves shown in Fig. 6. The TGA curve shows four stages of weight loss, with the initial stage showing a small weight loss of 8.29% observed below 100 °C which can be ascribed to the dehydration of the surface adsorbed water from the moisture content [51]. The second stage with the weight loss of 5.03% in the temperature range of 100–339 °C can be due to the loss of some oxygen atoms and bonded water molecules. The third stage of substantial weight loss of 18.54% observed between 340 and 600 °C can be attributed to the decomposition of the carbon material. The final stage of the weight loss of 7.83% can be ascertained to the release of lattice oxygen due to possible phase changes at high temperatures [52]. The total weight loss across the entire temperature range was 41.27%, showing that the MnO_2@rGO nanocomposite can withstand harsh conditions. The DTG peaks at 53.15 °C, 261.63 °C, 562.46 °C and 845.80 °C agreed with the four stages observed in the TGA curve.

3.7. Optimization of the adsorption processes

A central composite design was used for the optimization of the adsorption of methylene blue dye onto MnO_2@rGO. Three independent factors were optimized at 2 levels, namely (1) dosage, (2) sample pH and (3) sonication power. The design matrix was analyzed using the analysis of variance (ANOVA), response surface methodology and desirability function, the results are presented in Figs. 7–9, as a Pareto Chart, three dimensional plots and desirability profiles, respectively. The Pareto Chart (Fig. 7) of standardized effects was used to investigate statistical significances of the main effects (represented by horizontal bars). The bars were considered

Table 4
Adsorption isotherm constants for the adsorption of methylene blue on MnO_2@rGO nanocomposite.

Analyte	Langmuir isotherm				Freundlich isotherm			
	qmax (mg g^{-1})	KL (L g^{-1})	RL	R2	1/n	n	KF (L mg^{-1})	R2
Methylene Blue dye	156.25	0.0886	0.6796–0.0655	0.9901	0.55	1.83	15.89	0.9624
	Temkin isotherm				Dubinin–Radushkevich isotherm			
	BT (J mol^{-1})	KT (L g^{-1})	R2	qD-R (mg g^{-1})	E (KJ mol^{-1})	R2		
	85.74	1.20	0.9785	87.02	11.18	0.7851		
	Redlich-Peterson isotherm							
	KRP (L g^{-1})	β		αRP		R2		
	23.86	0.50		1.02		0.9465		

significant at 95% confidence level when they pass the redline which indicates a $p = 0.05$ [53]. In this study, the only factor that was found to be significant at 95% confidence level was sample pH. The sample pH could drive the behavior of both the adsorbent and adsorbate. The adsorbent was found to have a point of zero charge of 1.03 and 6.94.

The interactions between independent factors were investigated using 3-D surface plots. Fig. 8(a) shows the relationship between sample pH and adsorbent dosage on the percentage of analyte adsorbed. The interaction showed that at low pH and increasing dosage, the percentage of the adsorbed adsorbate increases towards a maximum. A similar trend was observed for the relationship between sample pH and sonication power (Fig. 8(b)). In contrast, Fig. 8(c) shows that the interaction between dosage and sonication power did not seem to have any quantitative result on the adsorptive recovery of the adsorbate.

The profiles for predicted values and desirability function on the Statistica software were used to estimate optimum conditions (Fig. 9a–d). The most desirable percentage adsorption (% Ads) was assigned a value of corresponding to a % Ads of 92%, a middle (42%) and least desirable (0%) were assigned 0.5 and 0.0 respectively [54,55]. According to Fig. 9a–d, the optimum conditions associated with a theoretical % Ads were an adsorbent dosage of 0.41 g L^{-1}, sample pH of 1.5 and up to 4.4 sonication power.

3.8. Adsorption isotherms

Adsorption isotherms are mathematical models used to describe how the adsorbent material interacts with the adsorbates when the adsorption process reaches the equilibrium state, established on a set of presumptions associated with how heterogenous or homogenous the solid surface might be and the type of coverage involved [56]. Due to complex adsorption system in liquid phase, a variety of isotherms were explored to find meticulous relationships between the dye in liquid phase and on the surface of the adsorbent material [57]. The isotherm models used to fit experimental data include two-parameter (Langmuir, Freundlich, Temkin, Dubinin-Radushkevich) and a three-parameter (Redlich-Peterson) isotherm model, as presented in Table 4. Using the following conditions in the adsorption experiments; pH = 1.5, sonication power = 4, dosage = 0.4 g L^{-1} and volume = 50 mL; the overall adsorption model was displayed in Fig. S1(a).

The Langmuir isotherm model (Fig. S1(b)) assumes that; (1) molecules are adsorbed at discrete active sites on the adsorbent surface, (2) each active site on the adsorbent adsorbs only one molecule, and when the available active sites are fully occupied, a maximum adsorption capacity is reached (3) The adsorbing surface on the adsorbent is generally uniform, (4) There is no interaction between the adsorbed molecules on the adsorbent surface [58]. The data in Table 4 confirm the monolayer adsorption of methylene blue dye onto MnO_2@rGO nanocomposite surface, with a high value of the coefficient of determination ($r^2 = 0.9901$). The Langmuir constant ($K_L = 0.09$) was consistent with the high adsorption capacity of 156 mg g^{-1} obtained, suggesting a strong affinity of the dye to the adsorption sites relative to a large surface area and pore volume, corroborating with the N_2 adsorption-desorption analysis results obtained [59,60]. The value of the separation factor (R_L) indicates the type of adsorption to be unfavourable ($R_L > 1$), favourable ($0 < R_L < 1.0$), linear ($R_L = 1.0$) or irreversible ($R_L = 0$) [60]. Thus, the R_L obtained in this study in the range 0.6796–0.0655 from low to high concentrations indicate that the adsorption of methylene blue onto the MnO_2@rGO nanocomposite surface is favourable.

The Freundlich isotherm model (Fig. S1(c)) is appropriate for the description of the adsorption process occurring on heterogeneous surfaces where the energy of the adsorption sites show an exponential distribution [59]. As indicated in Table 4, key Freundlich parameters such as K_F, and n were calculated as 15.89 mg g^{-1} and 1.83, respectively. Meanwhile, n indicates the intensity and feasibility of the adsorption process, with the n value in the range 1–10 indicating good adsorption characteristic and below 1 indicting poor adsorption characteristics [61]. Furthermore, the low 1/n below 1 indicates the favourable adsorption characteristics and validate the heterogeneity of the adsorbent material [56]. Thus, the 1/n and n values of 0.55 and 1.83 were obtained in this study, respectively, indicating favourable adsorption characteristics. However, the coefficient of determination in the Freundlich isotherm model for the adsorption of methylene blue onto the MnO_2@rGO nanocomposite surface is 0.9624, which is lower than that of the Langmuir isotherm. This indicates that the equilibrium data fitted well with the Langmuir isotherm.

The Temkin isotherm model (Fig. S1(d)) considers the influence of some indirect adsorbate-adsorbent interactions on the adsorption process, with the assumption that the heat of adsorption of all adsorbed molecules decreases linearly when the surface coverage increases [59,62]. The Temkin constant (B_T), which is related to the heat of sorption, and Temkin isotherm constant (K_T), which is the equilibrium binding constant; were calculated as 85.74 J mol^{-1} and 1.20 L g^{-1}, respectively. Based on the coefficient of determination ($r^2 = 0.9785$), it can be clearly seen that this model does not fit well with the equilibrium data when compared to the Langmuir isotherm, although it fits better than the Freundlich isotherm.

Table 5
Adsorption kinetic parameters for the adsorption of methylene blue on the MnO_2@rGO nanocomposite.

Pseudo-1st order model					
Intercept	**Slope**	**q_e (mg g^{-1})**	**$q_{e\ Exp}$ (mg g^{-1})**	**K_1**	**R^2**
2.1366	−0.0174	8.47	79.33	−0.00029	0.6411
Pseudo-2nd order model					
Intercept	**Slope**	**q_e (mg g^{-1})**	**$q_{e\ Exp}$ (mg g^{-1})**	**K_2**	**R^2**
0.0054	0.0131	76.34	79.33	0.048616	0.9999
Elovich model					
Intercept	**Slope**	**α**		**β**	**R^2**
63.75	3.209	45.32		0.31	0.8499
Intraparticle diffusion					
C		**K_{id}**		**R^2**	
60.39		3.271		0.9680	
74.64		0.1165		0.8229	

The Dubinin–Radushkevich (D-R) isotherm (Fig. S1(e)) is a model that is fundamentally capable of distinguishing between a chemical and a physical adsorption process resulting from the mean free energy of adsorption [59]. Consequently, the mean free energy (E) value below 8 kJ mol^{-1} demonstrates a physical adsorption process, whereas the E value between 8 and 16 kJ mol^{-1} demonstrates a chemical process [57]. As seen in Table 4, the E value obtained from the D-R isotherm is 11.18 kJ mol^{-1}, which indicates the chemisorption adsorption of methylene blue on MnO_2@rGO nanocomposite surfaces. As reflected by $r^2 = 0.7851$, the D-R isotherm is not the most ideal isotherm compared to Langmuir isotherm, however it serves a purpose of identifying the adsorption process type.

Redlich-Peterson (R–P) isotherm model (Fig. S1(f)) is a hybrid isotherm model featuring both the Langmuir and Freundlich isotherms in a three-parameter empirical equation. As shown in Table 4, Redlich-Peterson isotherm is comprised of three-parameters; K_{RP} (L g^{-1}) = 23.86, α_{RP} (L mg^{-1}) = 1.02 and β = 0.5. Accordingly, the constant β takes values between 0 and 1, but if β approaches 1, the model reduces to the Langmuir equation, and if β approaches 0, it reduces to the Freundlich equation [63]. Subsequently, Table 4 shows that a β value of 0.50 was obtained in this study, agreeing with the Langmuir isotherm. However, this model was not ideal in the overall fitting of the equilibrium data as it possessed a coefficient of determination of 0.9465 which was lower than that of the most ideal Langmuir isotherm, although it supported the Langmuir isotherm to describe the equilibrium interaction between methylene blue and MnO_2@rGO nanocomposite [56,64].

3.9. Adsorption kinetics

Kinetic studies provide valuable insights on the equilibrium adsorption rate, as well as the mechanism of the adsorption reaction. Following the equilibrium experiments using the optimum conditions of pH = 1.5, sonication power = 4, dosage = 0.4 g L^{-1} temperature = 25 ± 2 °C and volume = 50 mL, the overall adsorption kinetic model was presented in Fig. S2(a). It is noteworthy that the initial adsorption stage (0–25 min) is rapid due to the fast adsorption of the MB molecule on the active sites within the surface of the MnO_2@rGO nanocomposite. The second stage shows the equilibrium stage (25–60 min) which is a slow adsorption process due to the slow diffusion of MB molecules into the mesoporous structure of the adsorbent, identified on the N_2 adsorption-desorption analysis, as most adsorption sites have been occupied in the initial stage [65]. The high surface area, pore sizes and pore volume observed on the N_2 adsorption-desorption analysis and the single atom layered structure observed in FE-SEM results were highly beneficial for the speedy adsorption of MB on the MnO_2@rGO nanocomposite. Furthermore, the pseudo-first-order (Fig. S2(b)), pseudo-second-order (Fig. S2(c)), Elovich (Fig. S2(d)) and intraparticle diffusion (Fig. S2(e1 and e2)) were plotted, with the parameters and coefficients of determination shown in Table 5. Subsequently, for the adsorption process can be described by either the pseudo-first or second order equations; there should be a good linear relationship such that the trendline should pass through most of the points, the q_e (experimental) and q_e (calculated) should be close to each other and the R^2 should be close to 1 [6]. The pseudo-first order plot (Fig. S2(b)) shows that the linearity was poor with an R^2 of 0.6411 and a q_e of 8.47 which was not close to the experimental q_e of 79.33, indicating that the adsorption of MB onto MnO_2@rGO cannot be described by pseudo-first order model. However, the pseudo-second order plot (Fig. S2(c)) shows a good linearity with an R^2 of 0.999 and a q_e of 76.34 which was closer to the experimental q_e of 79.33 suggesting that the pseudo-second order mechanism was predominant for the adsorption of MB dye. The applicability of the model indicates that the adsorption of MB was driven by chemisorption, thus agreeing with the D-R isotherm model's findings. Fundamentally, it is known that the pseudo-first and second order kinetic models cannot identify the diffusion mechanisms, thus the intra-particle diffusion model was involved [56]. Subsequently, when the MB dye solution is mixed with the MnO_2@rGO nanocomposite adsorbent, transportation of the dye molecules from the solution through the interface region between the adsorbent and the solution occurs into the mesopores within the adsorbent material [66]. This creates a different pathway for the adsorptive removal of MB dye. The intra-particle diffusion plot (Fig. S2(e1 and e2)) shows that the intra-particle diffusion occurred in two stages, stage 1 (first linear portion) attributed to the most readily available sites on the adsorbent surface and stage 2 (second portion forming a plateau) ascribed to the diffusion through inner pores. Thus, the initial uptake of MB by MnO_2@rGO nanocomposite occur through surface diffusion process, whilst the latter part is controlled by pore diffusion [8,56,66]. The mesopore structure identified on the N_2 adsorption-desorption results play a major role in the pore diffusion process. The Elovich model (Fig. S2(d)) further confirmed that chemisorption described the uptake of MB by the

Table 6
Thermodynamic parameters for the adsorption of methylene blue on MnO_2@rGO nanocomposite.

Adsorbent	Temp (K)	q_e	Kc	ΔG° (KJ mol^{-1} K^{-1})	ΔH° (KJ mol^{-1})	ΔS° (J mol^{-1} K^{-1})	R^2
MnO_2@rGO nanocomposite	298	74.47	4.81	−3.89	26.83	63.09	0.9523
	303	75.83	5.18	−4.14			
	308	76.47	5.36	−4.31			
	313	76.96	5.51	−4.44			

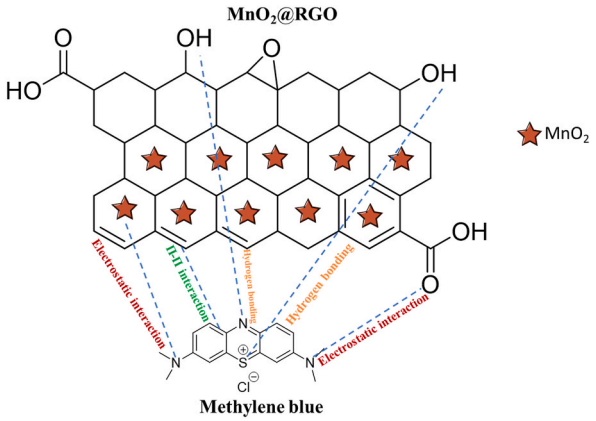

Scheme 2. Possible mechanism responsible for the adsorption of MB in the MnO_2@rGO nanocomposite.

MnO_2@rGO nanocomposite adsorbent with a good correlation coefficient.

3.10. Adsorption thermodynamics

As adsorption strongly relies on temperature, the thermodynamic investigations for the methylene blue adsorption on MnO_2@rGO nanocomposite were carried out to assess the feasibility of the adsorption process and the relevant mechanism of adsorption involved [67]. Thus, various temperatures ranging from 25 to 40 °C were investigated and key thermodynamic parameters including ΔG°, ΔH° and ΔS° were determined (Table 6). The Van Hoff linear plot of ln Kc versus 1/T was plotted (Fig. S3) and the slope and intercept were used to obtain the values of ΔH° (26.83 kJ mol^{-1}) and ΔS° (63.09 J mol^{-1} K^{-1}), respectively. The positive ΔH° value demonstrated the endothermic character of the adsorption process, and the positive ΔS° suggested an increase in randomness/disorder across the adsorbent-adsorbate interface during the adsorption process [64]. Furthermore, the negative values of ΔG° (−3.89 to −4.44 kJ mol^{-1} K^{-1}) suggest that the adsorption of methylene blue on MnO_2@rGO nanocomposite was spontaneous [67]. Interestingly, the ΔH° greater than 20.9 kJ mol^{-1} was deemed to render chemisorption mechanism as dominant [64], which is consistent with the ΔH° = 26.83 kJ mol^{-1} obtained in the study and agrees with the Dubinin–Radushkevich isotherm results. The Arrhenius equation (eq. (4)) was used to determine the activation energy (Ea) which was found to be −6.83 kJ mol^{-1}. The Ea was very small, with the negative value suggesting that the rise in solution temperature was not favourable for MB adsorption onto MnO_2@rGO nanocomposite [68]. Thus, the energy barriers are absent as there is a reduction in the probability of the colliding dye molecules being captured by the adsorbent [69].

$$In\ K_2 = In\ A - \frac{E_a}{RT} \tag{4}$$

where K is the rate constant, E_a is the activation energy (kJ mol^{-1}), R is the universal gas constant (8.314 J mol^{-1} K^{-1}), T is the absolute temperature (in K) and A is the Arrhenius factor (g mol^{-1} s^{-1}).

3.11. Adsorption mechanism

Insights on the possible interactions involved on the adsorption of methylene blue dye (chemical structure displayed in Fig. S4) onto MnO_2@rGO nanocomposite surface were explored. Subsequently, the pareto chart analysis identified the pH as the most significant factor on the adsorption of MB. Thus, the pH drift method was used to identify the point of zero charge (PZC), to understand the pH at which the adsorbent behave as a neutral species [27]. Interestingly, the PZC was obtained at 1.03 and 6.94 (Fig. S5), indicating that at the pH below the obtained PZC the surface charge on the adsorbent is positive, and at the pH above the obtained PZC the surface is negative [70]. The MB dye is cationic in solution and the optimum pH of 1.5 suggests that MB interacts favorably with the acidified surface of MnO_2@rGO nanocomposite via the electrostatic interaction. The FTIR was further deployed to study the

Table 7
The removal of MB in textile wastewater samples (n = 3).

Sample	Before adsorption (mg L^{-1})	After adsorption (mg L^{-1})	% RE
Influent textile wastewater	32.64 ± 0.34	0.57 ± 1.12	98.25
Effluent textile wastewater	33.68 ± 0.77	0.19 ± 0.81	99.43

Table 8
Comparison of the performance of various rGO-based adsorbents used for the removal of methylene blue in aqueous solutions.

Adsorbent	Analyte	pH	Dosage (g L^{-1})	Volume (mL)	Equilibrium time (min)	Adsorption capacity (mg g^{-1})	Reference (s)
Reduced graphene oxide (rGO)	Methylene blue	6.0	0.8	50	30	121.9	[73]
$MgFe_2O_4$/reduced graphene oxide	Methylene blue	8.0	2	50	60	21.0	[26]
Polyaniline/reduced graphene oxide (PANI/RGO)	Methylene blue	6.5	0.6	50	270	19.2	[74]
Ni@rGO	Methylene blue	8.3	0.2	50	45	946.1	[75]
MnO_2@rGO nanocomposite	Methylene blue	1.5	0.4	50	25	156.2	This work

interactions involved in MB adsorption as displayed in Fig. S6. The binding interaction (π-π stacking) existed between the aromatic rings of MB dye and rGO within the MnO_2@rGO nanocomposite as reflected by the shifting of the C═C band from 1580 to 1592 cm^{-1} [71,72]. Hydrogen bonding might also act as a predominant interaction following the immediate existence of a band around 1020 cm^{-1} that might be due to the aromatic or aliphatic amines leading to the interaction of the N atoms in MB and H atoms on the surface of the MnO_2@rGO nanocomposite [71]. It is noteworthy that the hydroxy (both OH and C–OH) and epoxy (C–O) groups which all appear to have shifted on the FTIR spectra of MnO_2@rGO nanocomposite are easily deprotonated to interact readily with N atoms in MB dye. The Mn–O bands from MnO_2 appear to have interacted with the OH in the MB dye via the electrostatic interactions. The CH and CH_2 bands appear to be more prominent after adsorption, suggesting the strong interaction between MB dye and MnO_2@rGO nanocomposite. The results confirm that chemisorption adsorption mechanism was dominant for the removal of MB using MnO_2@rGO nanocomposite, further agreeing with the D-R isotherm results. All the possible interactions involved in the adsorption of MB onto the MnO_2@rGO nanocomposite were illustrated in Scheme 2. The following mechanistic steps are therefore predicted:

[1] The movement of the of the MB dye from the solution to the surface of the MnO_2@rGO nanocomposite adsorbent,
[2] Adsorption of MB dye through active sites resulting from functional groups present on the surface of the MnO_2@rGO nanocomposite adsorbent,
[3] Diffusion of the MB dye through the mesopores on the MnO_2@rGO nanocomposite adsorbent structure.

3.12. Analysis of textile wastewater samples

The adsorptive removal of MB in spiked textile wastewater was carried out to evaluate the effectiveness of MnO_2@rGO nanocomposite in complex matrices. Using the obtained optimum conditions, the developed method resulted in high removal efficiency in the influent textile wastewater (98.25%) and effluent textile wastewater (99.43%), as presented in Table 7. The high percentage recoveries suggest that there were no interferences in the form of other constituents within the wastewater matrices that could hinder the removal of MB.

The performance of the synthesized MnO_2@rGO nanocomposite was compared with the previously reported rGO based adsorbents as presented in Table 8. Compared with other adsorbents, it is noteworthy that the synthesized MnO_2@rGO nanocomposite exhibited a relatively high adsorption ability, reaching equilibrium in an impressive time of 25 min. This could be ascribed to the improved adsorption kinetics emancipating from the highly porous surface, abundant surface-active sites and large surface area.

3.13. Regeneration and reusability of the spent adsorbent

The regeneration and reusability of the spent MnO_2@rGO nanocomposite adsorbent was studied by performing a sequence of adsorption-desorption experiments. Concisely, adsorption was carried out as previously described and desorption was carried out using 0.5 M HCl as a desorption medium [6,72]. After desorption, the spent adsorbent was washed with water, and then ethanol, before being dried overnight at 60 °C. The removal efficiency and adsorption capacity only reduced to 89% and 130 mg g^{-1}, respectively, after 8 cycles showing that MnO_2@rGO nanocomposite adsorbent can be successfully regenerated using HCl to desorb the adsorbed dye as shown in Fig. 10. The excellent performance and reusability of the MnO_2@rGO nanocomposite adsorbent paves new avenues for the removal of MB dye using a sustainable material.

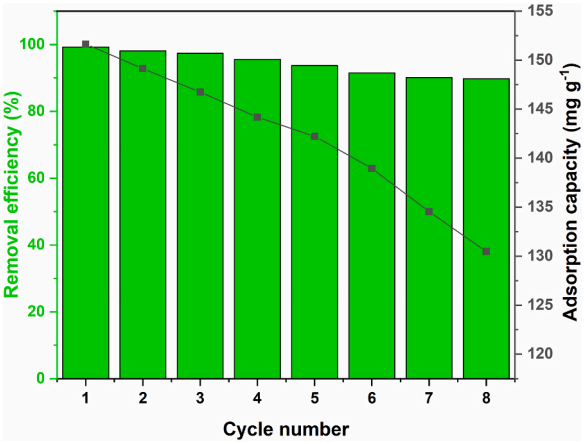

Fig. 10. The removal efficiencies and adsorption capacity after multiple adsorption-desorption cycles of MB using MnO_2@rGO nanocomposite adsorbent at pH 1.5, dosage of 0.4 g L^{-1}, volume of 50 mL and a concentration of 30 mg L^{-1}.

4. Conclusion

The feasibility of the adsorptive removal of methylene blue using MnO_2@rGO nanocomposite was investigated. Methylene blue was found to adsorb strongly on the surface of the MnO_2@rGO nanocomposite adsorbent, reaching equilibrium in just 25 min. The adsorption behavior was described by the monolayer Langmuir isotherm type, with the Dubinin–Radushkevich (D-R) isotherm confirming the chemisorption mechanism to be predominant for the adsorption of MB. The adsorption kinetics followed a pseudo-second order model, with the intra-particle diffusion as one of the rate-determining-step. The kinetics and thermodynamic data confirmed the chemisorption mechanism, which was explicitly configured following the hydrogen bonding and π-π stacking as predominant interactions on the MB adsorption process. The adsorption mechanisms involved suggested that the surface area, binding sites and pore diffusion were very important on the adsorption of MB onto MnO_2@rGO nanocomposite adsorbent. The high performance on the removal of MB in textile wastewater and the interesting regeneration-reusability suggest that MnO_2@rGO nanocomposite can be applied as an adsorbent even in matrices with various pollutants and reused many times without a significant loss in performance.

Funding statement

Financial support received from the Department of Science and Innovation-National Research Foundation South African Research Chairs Initiative (DSI-NRF SARChI) (grant no. 91230) is acknowledged.

Author contribution statement

Tshimangadzo S. Munonde: Conceived and designed the experiments; Performed the experiments; Analyzed and interpreted the data; Contributed reagents, materials, analysis tools or data; Wrote the paper.

Azile Nqombolo: Conceived and designed the experiments; Performed the experiments; Analyzed and interpreted the data.

Siphosethu Hobongwana: Conceived and designed the experiments; Performed the experiments; Contributed reagents, materials, analysis tools or data.

Anele Mpupa: Performed the experiments; Analyzed and interpreted the data; Contributed reagents, materials, analysis tools or data; Wrote the paper.

Philiswa N. Nomngongo: Conceived and designed the experiments; Analyzed and interpreted the data; Contributed reagents, materials, analysis tools or data; Wrote the paper.

Data availability statement

Data included in article/supplementary material/referenced in article.

Declaration of competing interest

The authors wish to declare that they have no competing interest both financially and personally.

Acknowledgments

The authors send their sincere gratitude to the University of Johannesburg (Department of Chemical Sciences), South Africa for

their support through facilities used in this study.

Appendix A. Supplementary data

Supplementary data to this article can be found online at https://doi.org/10.1016/j.heliyon.2023.e15502.

References

[1] A.A. Panhwar, K.F. Almani, A.A. Kandhro, Environmental degradation by textile industry; performance of chemical coagulants and activated carbon for removal of COD, BOD, Tech. J. 25 (2020) 16–20.
[2] G. Hole, A.S. Hole, Recycling as the way to greener production: a mini review, J. Clean. Prod. 212 (2019) 910–915.
[3] A.A. Inyinbor, F.A. Adekola, G.A. Olatunji, Kinetics, isotherms and thermodynamic modeling of liquid phase adsorption of Rhodamine B dye onto Raphia hookerie fruit epicarp, Water Resour. Ind. 15 (2016) 14–27.
[4] J. Cheng, C. Zhan, J. Wu, Z. Cui, J. Si, Q. Wang, X. Peng, L.-S. Turng, Highly efficient removal of methylene blue dye from an aqueous solution using cellulose acetate nanofibrous membranes modified by polydopamine, ACS Omega 5 (2020) 5389–5400.
[5] R.S.P. Mak, E.L. Liebelt, Methylene blue: an antidote for methemoglobinemia and beyond, Pediatr. Emerg. Care 37 (2021) 474–477.
[6] T.S. Munonde, N.P. September, A. Mpupa, P.N. Nomngongo, Two agitation routes for the adsorption of Reactive Red 120 dye on NiFe LDH/AC nanosheets from wastewater and river water, Appl. Clay Sci. 219 (2022), 106438.
[7] S. Dutta, J. Bhattacharjee, A comparative study between physicochemical and biological methods for effective removal of textile dye from wastewater, in: Development in Wastewater Treatment Research and Processes, Elsevier, 2022, pp. 1–21.
[8] W. Ruan, J. Hu, J. Qi, Y. Hou, C. Zhou, X. Wei, Removal of dyes from wastewater by nanomaterials: a review, Adv. Mater. Lett. 10 (2019) 9–20.
[9] B. Meroufel, O. Benali, M. Benyahia, Y. Benmoussa, M.A. Zenasni, Adsorptive removal of anionic dye from aqueous solutions by Algerian kaolin: characteristics, isotherm, kinetic and thermodynamic studies, J. Mater. Environ. Sci. 4 (2013) 482–491.
[10] A. Hamzezadeh, Y. Rashtbari, S. Afshin, M. Morovati, M. Vosoughi, Application of low-cost material for adsorption of dye from aqueous solution, Int. J. Environ. Anal. Chem. 102 (2022) 254–269.
[11] O. Hamdaoui, E. Naffrechoux, Modeling of adsorption isotherms of phenol and chlorophenols onto granular activated carbon: Part I. Two-parameter models and equations allowing determination of thermodynamic parameters, J. Hazard Mater. 147 (2007) 381–394.
[12] X. Tang, G. Ran, J. Li, Z. Zhang, C. Xiang, Extremely efficient and rapidly adsorb methylene blue using porous adsorbent prepared from waste paper: kinetics and equilibrium studies, J. Hazard Mater. 402 (2021), 123579.
[13] H.H.C. Lima, R.S. Maniezzo, M.E.G. Llop, V.L. Kupfer, P.A. Arroyo, M.R. Guilherme, A.F. Rubira, E.M. Girotto, A.W. Rinaldi, Synthesis and characterization of pecan nutshell-based adsorbent with high specific area and high methylene blue adsorption capacity, J. Mol. Liq. 276 (2019) 570–576.
[14] R.M. Novais, A.P.F. Caetano, M.P. Seabra, J.A. Labrincha, R.C. Pullar, Extremely fast and efficient methylene blue adsorption using eco-friendly cork and paper waste-based activated carbon adsorbents, J. Clean. Prod. 197 (2018) 1137–1147.
[15] A.H. Jawad, A.S. Abdulhameed, Mesoporous Iraqi red kaolin clay as an efficient adsorbent for methylene blue dye: adsorption kinetic, isotherm and mechanism study, Surface. Interfac. 18 (2020), 100422.
[16] B. Zheng, X. Lin, X. Zhang, D. Wu, K. Matyjaszewski, Emerging functional porous polymeric and carbonaceous materials for environmental treatment and energy storage, Adv. Funct. Mater. 30 (2020), 1907006.
[17] V.L.E. Siong, K.M. Lee, J.C. Juan, C.W. Lai, X.H. Tai, C.S. Khe, Removal of methylene blue dye by solvothermally reduced graphene oxide: a metal-free adsorption and photodegradation method, RSC Adv. 9 (2019) 37686–37695.
[18] J. Gaidukevic, R. Aukstakojyte, J. Barkauskas, G. Niaura, T. Murauskas, R. Pauliukaite, A novel electrochemical sensor based on thermally reduced graphene oxide for the sensitive determination of dopamine, Appl. Surf. Sci. 592 (2022), 153257.
[19] S.N. Alam, N. Sharma, L. Kumar, Synthesis of graphene oxide (GO) by modified hummers method and its thermal reduction to obtain reduced graphene oxide (rGO), Graphene 6 (2017) 1–18.
[20] N. Jahan, H. Roy, A.H. Reaz, S. Arshi, E. Rahman, S.H. Firoz, M.S. Islam, A comparative study on sorption behavior of graphene oxide and reduced graphene oxide towards methylene blue, Case Stud. Chem. Environ. Eng. 6 (2022), 100239.
[21] I. Chowdhury, N.D. Mansukhani, L.M. Guiney, M.C. Hersam, D. Bouchard, Aggregation and stability of reduced graphene oxide: complex roles of divalent cations, pH, and natural organic matter, Environ. Sci. Technol. 49 (2015) 10886–10893.
[22] N. Ye, Z. Wang, S. Wang, H. Fang, D. Wang, Aqueous aggregation and stability of graphene nanoplatelets, graphene oxide, and reduced graphene oxide in simulated natural environmental conditions: complex roles of surface and solution chemistry, Environ. Sci. Pollut. Res. 25 (2018) 10956–10965.
[23] J. Song, Y. Zeng, Y. Liu, W. Jiang, Retention of graphene oxide and reduced graphene oxide in porous media: diffusion-attachment, interception-attachment and straining, J. Hazard Mater. 431 (2022), 128635.
[24] N. Tara, S.I. Siddiqui, Q.-V. Bach, S.A. Chaudhry, Reduce graphene oxide-manganese oxide-black cumin based hybrid composite (rGO-MnO2/BC): a novel material for water remediation, Mater. Today Commun. 25 (2020), 101560.
[25] T. Chhabra, A. Kumar, A. Bahuguna, V. Krishnan, Reduced graphene oxide supported MnO2 nanorods as recyclable and efficient adsorptive photocatalysts for pollutants removal, Vacuum 160 (2019) 333–346.
[26] M. Adel, M.A. Ahmed, A.A. Mohamed, Synthesis and characterization of magnetically separable and recyclable crumbled MgFe2O4/reduced graphene oxide nanoparticles for removal of methylene blue dye from aqueous solutions, J. Phys. Chem. Solid. 149 (2021), 109760.
[27] S.H. Mnyipika, T.S. Munonde, P.N. Nomngongo, MnO2@ reduced graphene oxide nanocomposite-based electrochemical sensor for the simultaneous determination of trace Cd (II), Zn (II) and Cu (II) in water samples, Membranes (Basel) 11 (2021) 517.
[28] S. Yugambica, A.C. Dhanemozhi, Synthesis and characterization of MnO2/rGO nanocomposite for supercapacitors, Int. Res. J. Eng. Technol. 4 (2017) 486–491.
[29] D.P. Samal, Characterization and Study of Adsorption of Methylene Blue Dye using Activated Carbon, 2014. B. Tech thesis.
[30] Z. Mulushewa, W.T. Dinbore, Y. Ayele, Removal of methylene blue from textile waste water using kaolin and zeolite-x synthesized from Ethiopian kaolin, Environ. Anal. Heal. Toxicol. (2021) 36.
[31] P.A. Mikhaylov, M.I. Vinogradov, I.S. Levin, G.A. Shandryuk, A.V. Lubenchenko, V.G. Kulichikhin, Synthesis and characterization of polyethylene terephthalate-reduced graphene oxide composites, in: Proceedings of the IOP Conference Series: Materials Science and Engineering, vol. 693, IOP Publishing, 2019, 12036.
[32] S.A. Soomro, I.H. Gul, H. Naseer, S. Marwat, M. Mujahid, Improved performance of CuFe2O4/rGO nanohybrid as an anode material for lithium-ion batteries prepared via facile one-step method, Curr. Nanosci. 15 (2019) 420–429.
[33] X. Qiao, S. Liao, C. You, R. Chen, Phosphorus and nitrogen dual doped and simultaneously reduced graphene oxide with high surface area as efficient metal-free electrocatalyst for oxygen reduction, Catalysts 5 (2015) 981–991.
[34] G. Yasin, M. Arif, M. Shakeel, Y. Dun, Y. Zuo, W.Q. Khan, Y. Tang, A. Khan, M. Nadeem, Exploring the nickel–graphene nanocomposite coatings for superior corrosion resistance: manipulating the effect of deposition current density on its morphology, mechanical properties, and erosion-corrosion performance, Adv. Eng. Mater. 20 (2018), 1701166.
[35] B.S. Singu, K.R. Yoon, Synthesis and characterization of MnO2-decorated graphene for supercapacitors, Electrochim. Acta 231 (2017) 749–758.

[36] B. Huang, X. Zhang, J. Cai, W. Liu, S. Lin, A novel MnO2/rGO composite prepared by electrodeposition as a non-noble metal electrocatalyst for ORR, J. Appl. Electrochem. 49 (2019) 767–777.
[37] J. Mondal, S.K. Srivastava, δ-MnO2 nanoflowers and their reduced graphene oxide nanocomposites for electromagnetic interference shielding, ACS Appl. Nano Mater. 3 (2020) 11048–11059.
[38] D. Majumdar, Review on current progress of MnO2-based ternary nanocomposites for supercapacitor applications, Chemelectrochem 8 (2021) 291–336.
[39] B. Gupta, N. Kumar, K. Panda, V. Kanan, S. Joshi, I. Visoly-Fisher, Role of oxygen functional groups in reduced graphene oxide for lubrication, Sci. Rep. 7 (2017) 1–14.
[40] P.J. Pomonis, D.E. Petrakis, A.K. Ladavos, K.M. Kolonia, G.S. Armatas, S.D. Sklari, P.C. Dragani, A. Zarlaha, V.N. Stathopoulos, A.T. Sdoukos, A novel method for estimating the C-values of the BET equation in the whole range 0< P/Po< 1 using a Scatchard-type treatment of it, Microporous Mesoporous Mater. 69 (2004) 97–107.
[41] S. Lowell, J.E. Shields, M.A. Thomas, M. Thommes, S. Lowell, J.E. Shields, M.A. Thomas, M. Thommes, Surface area analysis from the Langmuir and BET theories, in: Charact. Porous Solids Powders Surf. Area, Pore Size Density, 2004, pp. 58–81.
[42] K.S.W. Sing, Reporting physisorption data for gas/solid systems with special reference to the determination of surface area and porosity (Recommendations 1984), Pure Appl. Chem. 57 (1985) 603–619.
[43] D. Khan, L. Qiu, C. Liang, K. Mirza, M. Kashif, B. Yang, K.L. Kra, Y. Wang, X. Li, Formation and distribution of different pore types in the lacustrine calcareous shale: insights from XRD, FE-SEM, and low-pressure nitrogen adsorption analyses, ACS Omega 7 (2022) 10820–10839.
[44] M. Ates, O. Kuzgun, M. Yildirim, H. Ozkan, rGO/MnO 2/Polyterthiophene ternary composite: pore size control, electrochemical supercapacitor behavior and equivalent circuit model analysis, J. Polym. Res. 27 (2020) 1–18.
[45] Z.-F. Liu, C.-Y. Zhu, Y.-W. Ye, Y.-H. Zhang, F. Cheng, H.-R. Li, Synergistic optimization strategy involving sandwich-like MnO2@ rGO and laponite-modified PAM for high-performance zinc-ion batteries and zinc dendrite suppression, ACS Appl. Mater. Interfaces 14 (2022) 25962–25971.
[46] A. Xie, H. Wang, Z. Zhu, W. Zhang, X. Li, Q. Wang, S. Luo, Mesoporous CeO2-α-MnO2-reduced graphene oxide composite with ultra-high stability as a novel electrode material for supercapacitor, Surface. Interfac. 25 (2021), 101177.
[47] D. Guo, S. Dou, X. Li, J. Xu, S. Wang, L. Lai, H.K. Liu, J. Ma, S.X. Dou, Hierarchical MnO2/rGO hybrid nanosheets as an efficient electrocatalyst for the oxygen reduction reaction, Int. J. Hydrogen Energy 41 (2016) 5260–5268.
[48] S. Wang, X. Li, M. Li, X. Li, X. Li, S. Li, Q. Zhang, H. Li, Self-assembled three-dimensional microporous rGO/PNT/Fe3O4 hydrogel sorbent for magnetic preconcentration of multi-residue insecticides, Appl. Sci. 10 (2020) 5665.
[49] U. Zubair, A. Anceschi, F. Caldera, M. Alidoost, J. Amici, C. Francia, M. Zanetti, F. Trotta, S. Bodoardo, N. Penazzi, Dual confinement of sulphur with rGO-wrapped microporous carbon from β-cyclodextrin nanosponges as a cathode material for Li–S batteries, J. Solid State Electrochem. 21 (2017) 3411–3420.
[50] W. Dong, L. Meng, X. Hong, S. Liu, D. Shen, Y. Xia, S. Yang, MnO2/rGO/CNTs framework as a sulfur host for high-performance Li-S batteries, Molecules 25 (2020) 1989.
[51] S. Ghasemi, S.R. Hosseini, O. Boore-Talari, Sonochemical assisted synthesis MnO2/RGO nanohybrid as effective electrode material for supercapacitor, Ultrason. Sonochem. 40 (2018) 675–685.
[52] Y. Meng, Y. Liu, J. He, X. Sun, A. Palmieri, Y. Gu, X. Zheng, Y. Dang, X. Huang, W. Mustain, Large scale synthesis of manganese oxide/reduced graphene oxide composites as anode materials for long cycle lithium ion batteries, ACS Appl. Energy Mater. 4 (2021) 5424–5433.
[53] K. Mogolodi Dimpe, A. Mpupa, P.N.P.N. Nomngongo, Microwave assisted solid phase extraction for separation preconcentration sulfamethoxazole in wastewater using tyre based activated carbon as solid phase material prior to spectrophotometric determination, Spectrochim. Acta Part A Mol. Biomol. Spectrosc. 188 (2018) 341–348, https://doi.org/10.1016/j.saa.2017.07.039.
[54] S. Khodadoust, H. Sadeghi, A.A. Pebdani, J. Mohammadi, A. Salehi, Optimization of ultrasound-assisted extraction of colchicine compound from Colchicum haussknechtii by using response surface methodology, J. Saudi Soc. Agric. Sci. 16 (2017) 163–170.
[55] G.P. Mashile, A. Mpupa, P.N. Nomngongo, In-syringe micro solid-phase extraction method for the separation and preconcentration of parabens in environmental water samples, Molecules 23 (2018), https://doi.org/10.3390/molecules23061450.
[56] N.C. Le, D. Van Phuc, Sorption of lead (II), cobalt (II) and copper (II) ions from aqueous solutions by γ-MnO2 nanostructure, Adv. Nat. Sci. Nanosci. Nanotechnol. 6 (2015), 25014.
[57] M.T. Amin, A.A. Alazba, M. Shafiq, Adsorptive removal of reactive black 5 from wastewater using bentonite clay: isotherms, kinetics and thermodynamics, Sustainability 7 (2015) 15302–15318.
[58] W. Ye, Y. Pan, L. He, B. Chen, J. Liu, J. Gao, Y. Wang, Y. Yang, Design with modeling techniques, in: Industrial Ventilation Design Guidebook, Elsevier, 2021, pp. 109–183.
[59] N. Ayawei, A.N. Ebelegi, D. Wankasi, Modelling and interpretation of adsorption isotherms, J. Chem. 2017 (2017).
[60] Y. Cai, L. Zheng, Z. Fang, Selective adsorption of Cu (II) from an aqueous solution by ion imprinted magnetic chitosan microspheres prepared from steel pickling waste liquor, RSC Adv. 5 (2015) 97435–97445.
[61] A.S. Gugushe, A. Nqombolo, P.N. Nomngongo, Application of response surface methodology and desirability function in the optimization of adsorptive remediation of arsenic from acid mine drainage using magnetic nanocomposite: equilibrium studies and application to real samples, Molecules 24 (2019) 1792.
[62] X. Li, G. Wang, W. Li, P. Wang, C. Su, Adsorption of acid and basic dyes by sludge-based activated carbon: isotherm and kinetic studies, J. Cent. South Univ. 22 (2015) 103–113.
[63] M. Belhachemi, F. Addoun, Comparative adsorption isotherms and modeling of methylene blue onto activated carbons, Appl. Water Sci. 1 (2011) 111–117.
[64] A. Mpupa, A. Nqombolo, B. Mizaikoff, P.N. Nomngongo, Enhanced adsorptive removal of β-estradiol from aqueous and wastewater samples by magnetic nano-Akaganeite: adsorption isotherms, kinetics, and mechanism, Processes 8 (2020) 1197.
[65] Y. Li, Q. Du, T. Liu, X. Peng, J. Wang, J. Sun, Y. Wang, S. Wu, Z. Wang, Y. Xia, Comparative study of methylene blue dye adsorption onto activated carbon, graphene oxide, and carbon nanotubes, Chem. Eng. Res. Des. 91 (2013) 361–368.
[66] T.R. Sahoo, B. Prelot, Adsorption processes for the removal of contaminants from wastewater: the perspective role of nanomaterials and nanotechnology, in: Nanomaterials for the Detection and Removal of Wastewater Pollutants, Elsevier, 2020, pp. 161–222.
[67] S. Raghav, D. Kumar, Adsorption equilibrium, kinetics, and thermodynamic studies of fluoride adsorbed by tetrametallic oxide adsorbent, J. Chem. Eng. Data 63 (2018) 1682–1697.
[68] M. Al-Ghouti, M.A.M. Khraisheh, M.N.M. Ahmad, S. Allen, Thermodynamic behaviour and the effect of temperature on the removal of dyes from aqueous solution using modified diatomite: a kinetic study, J. Colloid Interface Sci. 287 (2005) 6–13.
[69] J.H. Potgieter, C. Pardesi, S. Pearson, A kinetic and thermodynamic investigation into the removal of methyl orange from wastewater utilizing fly ash in different process configurations, Environ. Geochem. Health 43 (2021) 2539–2550.
[70] A.S. Gugushe, A. Mpupa, T.S. Munonde, L. Nyaba, P.N. Nomngongo, Adsorptive removal of Cd, Cu, Ni and Mn from environmental samples using Fe3O4-zro2@ APS nanocomposite: kinetic and equilibrium isotherm studies, Molecules 26 (2021) 3209.
[71] A.H. Jawad, A.S. Abdulhameed, L.D. Wilson, S.S.A. Syed-Hassan, Z.A. Alothman, M.R. Khan, High surface area and mesoporous activated carbon from KOH-activated dragon fruit peels for methylene blue dye adsorption: optimization and mechanism study, Chin. J. Chem. Eng. 32 (2021) 281–290.
[72] M.A. Al-Ghouti, R.S. Al-Absi, Mechanistic understanding of the adsorption and thermodynamic aspects of cationic methylene blue dye onto cellulosic olive stones biomass from wastewater, Sci. Rep. 10 (2020) 1–18.
[73] F. Arias Arias, M. Guevara, T. Tene, P. Angamarca, R. Molina, A. Valarezo, O. Salguero, C. Vacacela Gomez, M. Arias, L.S. Caputi, The adsorption of methylene blue on eco-friendly reduced graphene oxide, Nanomaterials 10 (2020) 681.
[74] E.A. El-Sharkaway, R.M. Kamel, I.M. El-Sherbiny, S.S. Gharib, Removal of methylene blue from aqueous solutions using polyaniline/graphene oxide or polyaniline/reduced graphene oxide composites, Environ. Technol. (2019).
[75] M.H. Calimli, M.S. Nas, H. Burhan, S.D. Mustafov, Ö. Demirbas, F. Sen, Preparation, characterization and adsorption kinetics of methylene blue dye in reduced-graphene oxide supported nanoadsorbents, J. Mol. Liq. 309 (2020), 113171.